Engineering Fracture Mechanics 192 (2018) 307–327

Contents lists available at ScienceDirect

Engineering Fracture Mechanics

journal homepage: www.elsevier.com/locate/engfracmech

An efficient mixed-mode rate-dependent cohesive fracture model using sigmoidal functions

Oliver Giraldo-Londoño [a], Daniel W. Spring [b], Glaucio H. Paulino [a,*], William G. Buttlar [c]

[a] School of Civil and Environmental Engineering, Georgia Institute of Technology, Atlanta, GA, United States
[b] The Equity Engineering Group, Inc., Shaker Heights, OH, United States
[c] School of Civil and Environmental Engineering, University of Missouri, Columbia, MO, United States

ARTICLE INFO

Article history:
Received 20 September 2017
Received in revised form 8 December 2017
Accepted 11 December 2017
Available online 15 December 2017

Keywords:
PPR cohesive zone model
Rate-dependent fracture
Damage mechanics
Viscoelastic CZM
Abaqus UEL

ABSTRACT

Rate-dependent fracture processes can be investigated by means of cohesive zone models (CZMs). For instance, one approach enhances existing CZMs with phenomenological expressions used to represent the fracture energy, cohesive strength, and/or maximum crack opening as a function of the crack opening rate. Another approach assumes a viscoelastic CZM in front of the crack tip. Although computationally less expensive, the former approach misses most of the physics driving the rate-dependent fracture process. The latter approach better represents the physics driving the rate-dependent fracture process, yet it is computationally more expensive. This work presents a methodology for studying mixed-mode rate-dependent fracture that is both efficient and approximates the viscoelastic material behavior in front of the crack tip. In this mixed-mode approach, we approximate the viscoelastic behavior in front of the crack tip using two rate-dependent springs. One spring acts in the normal direction to the crack plane, while the other acts in the tangential direction. In order to mimic a viscoelastic CZM, we assume that the stiffness of each spring is a function of the crack opening rate and enforce that their tractions are continuous with respect to changes in the crack opening rates. To account for damage, we scale the tractions from the rate-dependent springs using two damage parameters extracted from the Park-Paulino-Roesler (PPR) cohesive fracture model. The rate-dependent model is implemented as a user defined element (UEL) subroutine in Abaqus. While attaining a high level of accuracy, the present approach allows for significant savings in computational cost when compared with a CZM based on fractional viscoelastic theory.

1. Introduction

Significant theoretical developments to understand fracture in viscoelastic solids were introduced between the 1960s and 1980s. Schapery [1] developed a thermodynamics-based theory to analyze the thermo-mechanical behavior of viscoelastic solids, including a model for isothermal crack propagation that is based on an energy functional. Williams [2] proposed an extension of the Griffith fracture criterion for linearly viscoelastic solids that includes viscous dissipation. Wnuk and Knauss [3] studied propagation of a penny-shaped crack in a viscoelastic material by modeling the material in front of the crack tip using a viscoplastic cohesive-type model. The rate-dependent plastic model indicated that the time at which failure occurs is

* Corresponding author.
E-mail addresses: ogiraldo6@gatech.edu (O. Giraldo-Londoño), dspring_86@hotmail.com (D.W. Spring), paulino@gatech.edu (G.H. Paulino), buttlarw@missouri.edu (W.G. Buttlar).

https://doi.org/10.1016/j.engfracmech.2017.12.016
0013-7944/

smaller than that predicted by rate-independent plasticity. Mueller and Knauss [4] studied crack propagation on an infinitely long viscoelastic strip. Their work, which is an extension of the Irwin fracture criterion for linearly viscoelastic materials, led to predictions of crack propagation speeds which are in good agreement with experimental measurements. Schapery [5–7] studied crack initiation and growth in linearly viscoelastic media using a model based on the concept of cohesive zone models for both linear materials [8,9] and viscoelastic materials [3,4,10,11]. The study by Schapery found that crack growth was affected by the fracture energy and stress distribution in the fracture process zone, both of which can be rate-dependent. Schapery [12] used the correspondence principle to develop a time-dependent version of the *J* integral [13] that is applicable to nonlinear viscoelastic solids. These classical works have set the stage for more recent developments focused on numerical investigation of rate-dependent fracture phenomena.

Cohesive zone models (CZMs) have been applied to numerically investigate the rate-dependent fracture process of many materials. For instance, CZMs have been used for rate-dependent fracture simulations of polymers [14,15], acrylics [16], adhesives [17–20], asphalt concrete [21–23], and concrete [24]. These fracture simulations are typically conducted using the finite element (FE) method, such that CZMs are used to represent the nonlinear behavior in front of the crack tip by means of zero-thickness cohesive elements that follow a governing traction-separation relation [25]. To accurately model rate-dependent fracture processes, it is important that the traction-separation relation adequately represents the rate-dependent bond-breakage in front of the crack tip. Developing rate-dependent traction-separation relations is typically achieved using two approaches. The first approach consists of using phenomenological expressions that express the fracture energy, cohesive strength and/or maximum crack opening as a function of the crack opening rate [16–18,20,23,26–32], while the second approach consists of using a viscoelastic material model to represent the material in front of the crack tip [14,19,21,33–37]. The former approach, although computationally less expensive, ignores most of the underlying physical mechanisms causing the fracture process to be rate-dependent. The latter approach is more expensive, yet it more accurately approximates the physics of rate-dependent fracture.

A rate-dependent CZM that is both efficient and able to accurately approximate the physics of rate-dependent fracture is of primary interest to the computational fracture mechanics community. In order to derive a model with these two qualities, we analyze the behavior of CZMs that use a viscoelastic material in front of the crack tip and then mimic the behavior of this material using a simplified model. An example of a viscoelastic CZM is that proposed by Bažant and Li [38,39]. In their study, they present a rate-dependent CZM using a nonlinear Kelvin-Voigt model, in which the elastic spring is replaced by a nonlinear softening spring. Other CZMs have used a standard linear solid (SLS) model to represent the material in the fracture process zone (FPZ) [19,34,35,40]. The model by Xu et al. [34,35] replaces the elastic arm of the SLS model with a nonlinear spring with exponential softening. Their model predicts that both the cohesive strength and fracture energy grow as the crack opening rate increases. Another model using a SLS model in front of the crack tip was presented in a study by Musto and Alfano [19]. In their work, they use a scalar damage parameter consistent with a bilinear CZM to scale the undamaged tractions from a SLS model. Using their CZM, they were able to approximate experimental results obtained from double cantilever beam (DCB) tests performed at several constant loading rates. After comparing their numerical and experimental results, Musto and Alfano [19] found that their model approximated the experimental only for a narrow range of loading rates. Recently, Musto and Alfano [36] improved their previous model [19] by using a version of a SLS model based on fractional viscoelastic theory [41]. After comparing their numerical and experimental results, Musto and Alfano [36] found that with their new model they were able to accurately capture the experimental data for a range of loading rates that spanned around six orders of magnitude.

Cohesive zone models such as that presented in the work by Musto and Alfano [36] predict that both the local fracture energy and cohesive strength grow as a sigmoidal function of the crack opening rate. This sigmoidal behavior has been experimentally observed by Marzi et al. [18] in rate-dependent debonding tests performed on a structural adhesive. The same sigmoid-like behavior for the fracture energy and cohesive strength is observed in a recent study by Giraldo-Londoño et al. [42]. In their study, they extend the work by Musto and Alfano [36] to account for mixed-mode fracture. Their study also considers the shape of the traction-separation relation, which is important in fracture simulations because the shape of the CZM can significantly affect the simulated global fracture behavior in the structure [43,44]. To account for the shape of the CZM, the model by Giraldo-Londoño et al. [42] uses damage parameters [45] extracted from the Park-Paulino-Roesler (PPR) cohesive zone model [46]. The ability to control the softening shape of the traction-separation relations under mixed-mode conditions allows their model to be general enough to model the fracture behavior of an arbitrary material [47].

The mixed-mode rate-dependent CZM presented by Giraldo-Londoño et al. [42] has shown promise to accurately model rate-dependent fracture phenomena for a wide range of loading rates. The ability of their model to accuracy simulate rate-dependent fracture relies on the fractional viscoelastic model. However, obtaining the tractions from a fractional viscoelastic model becomes computationally expensive because one has to evaluate a convolution integral at each time step [41], which becomes more expensive as the number of time steps increases. Although several numerical methods have been proposed to solve equations involving fractional differential operators [e.g., see 48–54], due to the non-locality of fractional derivatives, their numerical computation has, thus far, been expensive. To circumvent this issue, we present an approach in which we approximate the response of the fractional viscoelastic model [42] in a simplified way that requires no evaluation of convolution integrals.

More specifically, this paper presents a mixed-mode rate-dependent CZM that approximates the behavior of a viscoelastic media in front of the crack tip using two rate-dependent springs, one acting in the normal and the other in the tangential

direction to the crack plane. To resemble the viscoelastic material behavior, the traction-separation relations of the springs are forced to be continuous with respect to changes in the crack opening rates. To account for softening, the tractions obtained from the rate-dependent springs are scaled by two damage parameters that are obtained from the Park-Paulino-Roesler CZM [45,46]. The damage parameters are such that they increase monotonically, a condition that must be met if no self-healing takes place during the fracture process [55–58]. We demonstrate that the present model possesses a level of accuracy that is comparable to more sophisticated formulations based on viscoelastic models of fractional order [36,42], yet it is computationally efficient. Specifically, the savings in computational cost are achieved by avoiding evaluation of the convolution integrals, as in the case of the aforementioned fractional viscoelastic cohesive models.

The remainder of this paper is organized as follows. The derivation of the mixed-mode rate-dependent CZM is outlined in Section 2. Two comprehensive examples are discussed in detail in Section 3, followed by an analysis of the computational cost of the model in Section 4. Finally, the conclusions from this work are reviewed in Section 5.

2. Formulation of the rate-dependent CZM using sigmoidal functions

This section outlines the derivation of our proposed rate-dependent CZM, which is formulated in the framework of damage mechanics [59,60]. First, we derive undamaged tractions S_k from a rate-dependent spring model. Then, we scale the undamaged rate-dependent tractions using damage parameters d_k that are obtained from the PPR CZM. This yields rate-dependent cohesive tractions T_k, wherein the subscript k in the following derivation of the model takes values n and t to refer to the normal and tangential directions, respectively. The rate-dependent cohesive tractions are obtained as follows:

$$T_k\left(\Delta_k(t),\dot{\Delta}_k(t)\right) = [1 - d_k(\kappa_n,\kappa_t)]S_k\left(\Delta_k(t),\dot{\Delta}_k(t)\right). \tag{1}$$

The undamaged tractions and damage parameters in Eq. (1) are discussed in detail in the following two subsections.

2.1. Undamaged tractions

The undamaged tractions, S_k, are derived from a model using two rate-dependent springs.[1] One of the springs acts in the direction normal to the crack face and the other in the direction tangential to the crack face. For both rate-dependent spring models, we enforce the tractions to be continuous with respect to changes in the crack opening rates. We enforce the continuity condition, as illustrated in Fig. 1, to mimic the behavior of a viscoelastic material. From the continuity condition, the undamaged traction in the normal and tangential directions take the form

$$S_k\left(\Delta_k(t),\dot{\Delta}_k(t)\right) = \int_0^t \dot{\Delta}_k(\tau)\tilde{E}_k\left(\left|\dot{\Delta}_k(\tau)\right|\right)\mathrm{d}\tau, \quad (k = n,t), \tag{2}$$

or in a discrete form[2]

$$S_k\left(\Delta_k(t),\dot{\Delta}_k(t)\right) = S_k\left(\Delta_k(t_{N-1}),\dot{\Delta}_k(t_{N-1})\right) + \tilde{E}_k\left(\left|\dot{\Delta}_k(t)\right|\right)[\Delta_k(t) - \Delta_k(t_{N-1})], \quad (k = n,t), \tag{3}$$

where the values evaluated at t_{N-1} correspond to the tractions at the previous time increment (in a nonlinear FE context) [61]. The form of the tractions given by Eq. (3), indicates that only tractions and displacements from the previous time step are required to compute the tractions at the current time step. This saves significant computational cost compared to viscoelastic CZMs such as those in Refs. [36,42] (details of the model in Ref. [42] are summarized in Appendix A).

To complete our rate-dependent spring model, we need an expression for the rate-dependent spring stiffness, $\tilde{E}_k$. In this work, we propose the stiffness of the springs to be defined by the following sigmoidal functions of the crack opening rates:

$$\frac{\tilde{E}_k\left(\dot{\Delta}_k(t)\right)}{E_k} = f_k\left(\dot{\Delta}_k(t)\right) = 1 + (\beta_k - 1)\left[\frac{\left(\dot{\Delta}_k(t)/\dot{\Delta}_{k_0}\right)^p}{1 + \left(\dot{\Delta}_k(t)/\dot{\Delta}_{k_0}\right)^p}\right], \quad (k = n,t), \tag{4}$$

where E_k are the slow-limit stiffness, β_k are the fast-to-slow limit stiffness ratios, $\beta_k E_k$ are the fast-limit stiffness, $\dot{\Delta}_{k_0}$ are reference rates, and p is an exponent indicating the rate at which the respective stiffness transitions from slow-limit to fast-limit behavior. The terms slow-limit and fast-limit refer to the behavior as $\dot{\Delta}_k \to 0$ and $\dot{\Delta}_k \to \infty$, respectively. The rate-dependence of stiffness given by Eq. (4) is depicted in Fig. 2. As will be discussed in Section 2.3, the stiffness $\tilde{E}_k$ given by Eq. (4) leads to a sigmoidal form for the fracture energy and cohesive strength, in accordance with previous studies [36,42].

[1] Although the term "*spring*" is typically used to represent responses of the form force vs. displacement, such term is used in this study to represent a response of the form traction vs. crack opening displacement (e.g., see Fig. 1).

[2] The discrete form given by Eq. (3) is obtained by applying the backward Euler method to the time derivative of Eq. (2).

2.2. Normal and tangential damage parameters

To account for damage, the undamaged tractions given by Eq. (3) are scaled by two damage parameters d_k. We obtain the damage parameters from the PPR cohesive zone model [46], as presented by Spring et al. [45]:

$$d_k(\kappa_n,\kappa_t) = 1 - \frac{\hat{T}_k(\kappa_n,\kappa_t)}{E_k\kappa_k}, \quad (k = n,t). \tag{5}$$

The terms $\hat{T}_k(\kappa_n,\kappa_t)$ are the rate-independent normal and tangential cohesive tractions from the original PPR model [46], i.e.,

$$\hat{T}_n(\kappa_n,\kappa_t) = \frac{\Gamma_n}{\delta_n}\left[m\left(1-\frac{\kappa_n}{\delta_n}\right)^{\alpha}\left(\frac{m}{\alpha}+\frac{\kappa_n}{\delta_n}\right)^{m-1} - \alpha\left(1-\frac{\kappa_n}{\delta_n}\right)^{\alpha-1}\left(\frac{m}{\alpha}+\frac{\kappa_n}{\delta_n}\right)^{m}\right] \times \left[\Gamma_t\left(1-\frac{\kappa_t}{\delta_t}\right)^{\beta}\left(\frac{n}{\beta}+\frac{\kappa_t}{\delta_t}\right)^{n} + \langle\phi_t-\phi_n\rangle\right], \tag{6}$$

$$\hat{T}_t(\kappa_n,\kappa_t) = \frac{\Gamma_t}{\delta_t}\left[n\left(1-\frac{\kappa_t}{\delta_t}\right)^{\beta}\left(\frac{n}{\beta}+\frac{\kappa_t}{\delta_t}\right)^{n-1} - \beta\left(1-\frac{\kappa_t}{\delta_t}\right)^{\beta-1}\left(\frac{n}{\beta}+\frac{\kappa_t}{\delta_t}\right)^{n}\right] \times \left[\Gamma_n\left(1-\frac{\kappa_n}{\delta_n}\right)^{\alpha}\left(\frac{m}{\alpha}+\frac{\kappa_n}{\delta_n}\right)^{m} + \langle\phi_n-\phi_t\rangle\right]. \tag{7}$$

As discussed by Spring et al. [45], the values of E_n and E_t correspond to the initial normal and tangential stiffness of the PPR cohesive model, respectively. That is,

$$E_n = \frac{\partial\hat{T}_n}{\partial\kappa_n}(0,0) = -\frac{\Gamma_n}{\delta_n^2}\left(\frac{m}{\alpha}\right)^{m-1}(m+\alpha)\left[\Gamma_t\left(\frac{n}{\beta}\right)^{n} + \langle\phi_t-\phi_n\rangle\right], \tag{8}$$

$$E_t = \frac{\partial\hat{T}_t}{\partial\kappa_t}(0,0) = -\frac{\Gamma_t}{\delta_t^2}\left(\frac{n}{\beta}\right)^{n-1}(n+\beta)\left[\Gamma_n\left(\frac{m}{\alpha}\right)^{m} + \langle\phi_n-\phi_t\rangle\right]. \tag{9}$$

The PPR parameters α and β control the shape of the normal and tangential softening portions of the PPR cohesive tractions, respectively. Note that $\alpha \geqslant 1$ and $\beta \geqslant 1$. The terms m and n depend on α and β and the two initial slope indicators, λ_n and λ_t, as follows:

$$m = \frac{\alpha(\alpha-1)\lambda_n^2}{(1-\alpha\lambda_n^2)}, \quad n = \frac{\beta(\beta-1)\lambda_t^2}{(1-\beta\lambda_t^2)}. \tag{10}$$

The initial slope indicators, λ_n and λ_t, are given by

$$\lambda_n = \delta_{nc}/\delta_n, \quad \lambda_t = \delta_{tc}/\delta_t, \tag{11}$$

where δ_{nc} and δ_{tc} are the crack opening widths at which the peak tractions in the normal and tangential directions are reached, and δ_n and δ_t are

$$\delta_n = \frac{\phi_n}{\sigma_{\max}}\alpha\lambda_n(1-\lambda_n)^{\alpha-1}\left(\frac{\alpha}{m}+1\right)\left(\frac{\alpha}{m}\lambda_n+1\right)^{m-1}, \tag{12}$$

$$\delta_t = \frac{\phi_t}{\tau_{\max}}\beta\lambda_t(1-\lambda_t)^{\beta-1}\left(\frac{\beta}{n}+1\right)\left(\frac{\alpha}{n}\lambda_t+1\right)^{n-1}. \tag{13}$$

From the original presentation of the PPR model [46], when the normal and tangential fracture energies are different ($\phi_n \neq \phi_t$), the energy constants Γ_n and Γ_t are given by

$$\Gamma_n = (-\phi_n)^{\langle\phi_n-\phi_t\rangle/(\phi_n-\phi_t)}\left(\frac{\alpha}{m}\right)^{m}, \quad \Gamma_t = (-\phi_t)^{\langle\phi_t-\phi_n\rangle/(\phi_t-\phi_n)}\left(\frac{\beta}{n}\right)^{n}, \tag{14}$$

and when the normal and tangential fracture energies are the same ($\phi_n = \phi_t$), these energy constants are given by

$$\Gamma_n = -\phi_n\left(\frac{\alpha}{m}\right)^{m}, \quad \Gamma_t = \left(\frac{\beta}{n}\right)^{n}. \tag{15}$$

where the Macaulay bracket $\langle\cdot\rangle$ is defined as

$$\langle x\rangle = \begin{cases} 0 & x < 0 \\ x & x \geqslant 0 \end{cases}. \tag{16}$$

We use two kinematic quantities κ_n and κ_t in the calculation of the damage parameters, d_k, in Eq. (5). The values of κ_n and κ_t represent the historic maximum normal crack opening width, and the historic maximum absolute tangential crack opening width, respectively. As discussed by Spring et al. [45], these kinematic quantities must satisfy

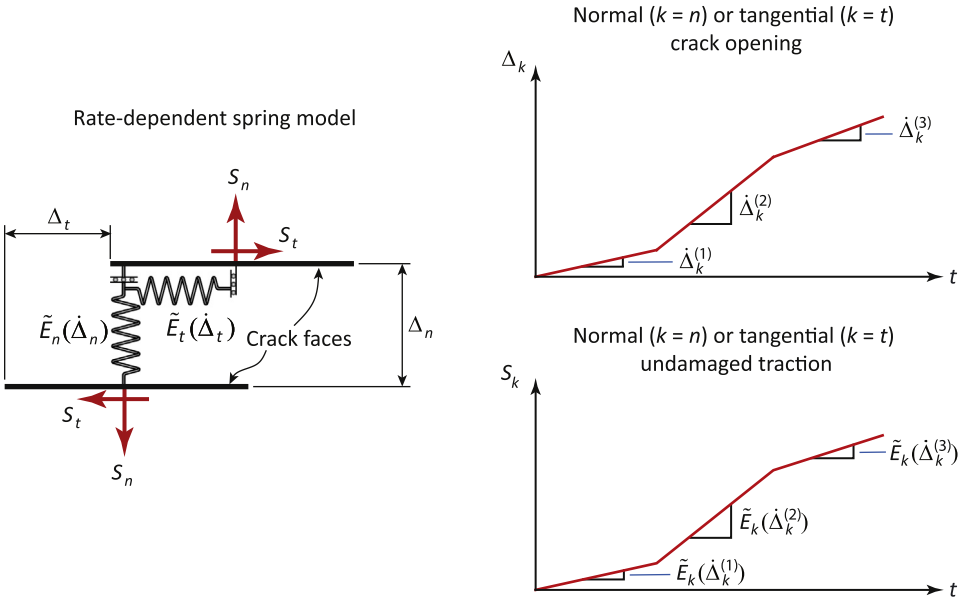

Fig. 1. Two rate-dependent springs (left) are used to obtain the undamaged tractions, S_k (right). As observed on the right side of the figure, the tractions S_k are assumed to be continuous with respect to changes in the crack opening rates, $\dot{\Delta}_k$. The subscript k in the figure takes the values $k = n$ and $k = t$ to refer to the normal and tangential directions, respectively.

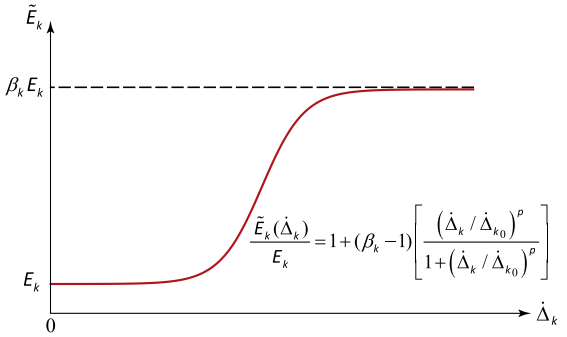

Fig. 2. Stiffness of the springs as a function of the crack opening rates. Two springs are used, one in the normal direction ($k = n$) and one in the tangential direction ($k = t$). The horizontal axis is in logarithmic scale.

$$\kappa_n^N = \max\left\{\kappa_n^{N-1}, \Delta_n^N\right\} \quad \text{and} \quad \kappa_t^N = \max\left\{\kappa_t^{N-1}, \left|\Delta_t^N\right|\right\}, \tag{17}$$

to guarantee a monotonic increase of the damage parameters throughout the loading history. This is a required condition if it is assumed that no self-healing occurs during the fracture process. The superscripts $N-1$ and N represent the solutions at increment $N-1$ and N in a nonlinear FE analysis. Although it is beyond the scope of the current work, healing can be added to the proposed framework using a healing variable such as that in used in Ref. [62]. Healing is an important mechanism to consider when modeling some time-dependent materials, such as asphalt [62–64] and polymers [65–68].

2.3. Rate-dependent cohesive tractions and fracture energy

To obtain expressions for the mixed-mode rate-dependent cohesive tractions, we substitute Eqs. (3) and (5) into Eq. (1), yielding

$$T_k\left(\Delta_k(t), \dot{\Delta}_k(t)\right) = \frac{\hat{T}_k(\kappa_n, \kappa_t)}{E_k \kappa_k}\left\{S_k\left(\Delta_k(t_{N-1}), \dot{\Delta}_k(t_{N-1})\right) + \tilde{E}_k\left(\left|\dot{\Delta}_k(t)\right|\right)[\Delta_k(t) - \Delta_k(t_{N-1})]\right\}. \tag{18}$$

Analytical expressions for the normal and tangential fracture energy and cohesive strength, as a function of the crack opening rate, can be directly obtained from Eq. (18). For instance, if one assumes monotonic loading conditions and constant crack opening rates, Eq. (18) simplifies to

$$T_k(\Delta_n, \Delta_t) = f_k\left(\dot{\Delta}_k\right)\hat{T}_k(\Delta_n, \Delta_t). \tag{19}$$

This simplification is possible because the kinematic quantities and the undamaged tractions become $\kappa_k = \Delta_k$ and $S_k = f_k\left(\dot{\Delta}_k\right)E_k\Delta_k$, respectively, where $f_k\left(\dot{\Delta}_k\right)$ is obtained from Eq. (4). Because the rate dependent tractions given by Eq. (19) are equal to a scalar multiple of the PPR cohesive tractions, $\hat{T}_k$, we are able to obtain analytical expressions for the fracture energy and cohesive strength for any constant crack opening rate. The resulting fracture energies are

$$G_k\left(\dot{\Delta}_k\right) = f_k\left(\dot{\Delta}_k\right)\phi_k, \tag{20}$$

and cohesive strengths are

$$T_k^{\max}\left(\dot{\Delta}_k\right) = f_k\left(\dot{\Delta}_k\right)T_{k_0}^{\max}, \tag{21}$$

where ϕ_k $(k = n, t)$ are the rate-independent cohesive fracture energies [46]. Moreover, the values of $T_{k_0}^{\max}$ are equal to the rate-independent cohesive strengths from the PPR cohesive model, i.e., $T_{n_0}^{\max} = \sigma_{\max}$ and $T_{t_0}^{\max} = \tau_{\max}$ [46].

The mode I fracture energy and cohesive strength from Eqs. (20) and (21) are compared with the values obtained from the fractional viscoelastic CZM presented by Giraldo-Londoño et al. [42], for a wide range of crack opening rates, in Fig. 3. An overview of the fractional model by Giraldo-Londoño et al. [42] is provided in Appendix A. To obtain the fracture energy and cohesive strength using the fractional CZM [42], the cohesive tractions were calculated via Eq. (45) using 200 time increments between $t = 0$ and $t = t_c$, where t_c is the time at which the tractions vanish. The fracture energies were obtained by numerical integration (using the trapezoidal rule) and the cohesive strengths were obtained as the maximum traction under the traction-separation curves. From Fig. 3a and b, it is observed that the fracture energy and cohesive strength calculated via Eqs. (20) and (21) are very close to those obtained from the fractional viscoelastic CZM [42]. The accuracy of the computed fracture energies and cohesive strengths is measured using relative percent error values. The percent error for fracture energy and cohesive strength are obtained as

$$\epsilon(G_n) = \frac{G_n^{\text{sigmoidal}} - G_n^{\text{fractional}}}{G_n^{\text{fractional}}} \times 100, \text{ and } \epsilon(T_n^{\max}) = \frac{T_n^{\max,\text{sigmoidal}} - T_n^{\max,\text{fractional}}}{T_n^{\max,\text{fractional}}} \times 100, \tag{22}$$

respectively. From Fig. 3c, we find that the maximum difference between both models is less than 1.2%. The computed percent differences are assessed relative to another model and not to experimental results. Therefore, the 1.2% in relative error is interpreted as a verification of accuracy of the model. The ability of the model to predict experimental results will be assessed in Section 3.1.

We further verify the accuracy of the model by comparing the cohesive tractions predicted by the model against those from the cohesive zone model of Ref. [42] (see Appendix A) for a general crack opening path. For simplicity purposes, the crack faces are assumed to remain parallel. The normal and tangential crack opening widths are assumed to be independent of each other, and follow the relations

$$\Delta_n(t) = t[1 - \cos(15t)], \quad \text{and} \quad \Delta_t(t) = 1.5t\sin(10t). \tag{23}$$

The normal and tangential crack opening widths given in Eq. (23) are illustrated in Fig. 4 for time $t \leqslant 3$ s. This time interval is chosen to ensure that the crack opening widths are large enough to produce complete failure of the cohesive element.

The cohesive tractions obtained for the crack opening path given by Eq. (23) are illustrated in Fig. 5. Note that the cohesive tractions obtained from the present formulation are very close to those obtained from the fractional viscoelastic model in [42], which reassures the accuracy of the present rate-dependent CZM. To find the rate-dependent cohesive tractions using our CZM, we only need to store the tractions obtained from the previous time step, in contrast to more accurate CZMs based on fractional viscoelastic theory [36,42], in which we often need to store the tractions from all previous time steps in order to find the tractions in the current time step. Savings in storage are an advantage of the present formulation, as it can be implemented to solve large-scale problems involving a large number of cohesive elements with a relatively lower computational cost.

2.3.1. Some comments on the rate dependence of fracture energy

Rate dependency can affect different materials in different ways. For instance, the fracture energy in rubbery materials increases with an increase in rate, while glassy materials may exhibit a decrease in fracture energy with an increase in rate. Several studies have shown that the fracture energy in elastomeric and other soft materials increases exponentially with crack speed. For instance, Zhou et al. [16] present experimental results for high-speed crack propagation of pre-strained PMMA plates showing an exponential growth of the fracture energy as the crack speed increases. Nearly exponential growth of fracture energy was also reported by Gent [69] during peeling tests conducted on polybutadiene elastomers in a rubbery

state (which was numerically verified by Rahul-Kumar et al. [15]), and by Kazerani et al. [29] during fracture tests of PMMA plates. Marzi et al. [18] show that the fracture energy in structural adhesive joints increases in a sigmoid-like fashion after performing several experiments over a wide range of strain rates. This sigmoidal behavior has also been observed analytically [36,40]. In addition, a recent study by Giraldo-Londoño et al. [42], used a fractional calculus based viscoelastic CZM that predicts a sigmoid-like behavior for both the mode I and II fracture energies and cohesive strengths. In agreement with experimental and numerical observations for rubbery materials, Eqs. (20) and (21) lead to a sigmoid-like shape for the fracture energies and cohesive strengths, justifying the use of Eq. (4) to define the stiffness of the rate-dependent springs for these types of materials.

Although the sigmoid-like behavior for the fracture energy that is predicted by our model is useful to simulate fracture in rubbery materials, it may be inadequate to simulate the fracture behavior of glassy polymers. The main reason for the inadequacy is that in glassy polymers the fracture energy has been observed to be non-monotonic with respect to the crack opening rates. That is, in glassy polymers the fracture energy may increase up to a certain value of crack opening rate and decrease afterwards. For some materials, such as asphalt concrete, which becomes glassy at low temperatures and high loading rates, experimental results have shown that fracture energy decreases with increasing loading rate [70]. Several authors have given different interpretations to the non-monotonic behavior of fracture energy versus crack opening rate that occurs in glassy polymers. For example, Williams [71] studied thermomechanical effects on crack propagation in PMMA and proposed that the non-monotonicity could be attributed to thermal softening in the fracture process zone. Thermal softening can be caused by increasing temperatures in front of the crack tip, which become more prominent as the crack speed increases. Johnson and Radon [72], explained the non-monotonicity in PMMA in the context of molecular kinetics. In their study, they indicated that the non-monotonic behavior of fracture energy was attributed to mobility changes in parts of the polymer molecule, which can be attributed to an adiabatic fracture behavior as the crack speed increases. Maugis [73] attributed the non-monotonic rate-dependent response of the fracture energy to viscoelastic losses at the crack tip, which are related to the loss modulus of the material in the fracture process zone. Such a model can be used to explain stick-slip motion, which is observed in glassy materials.

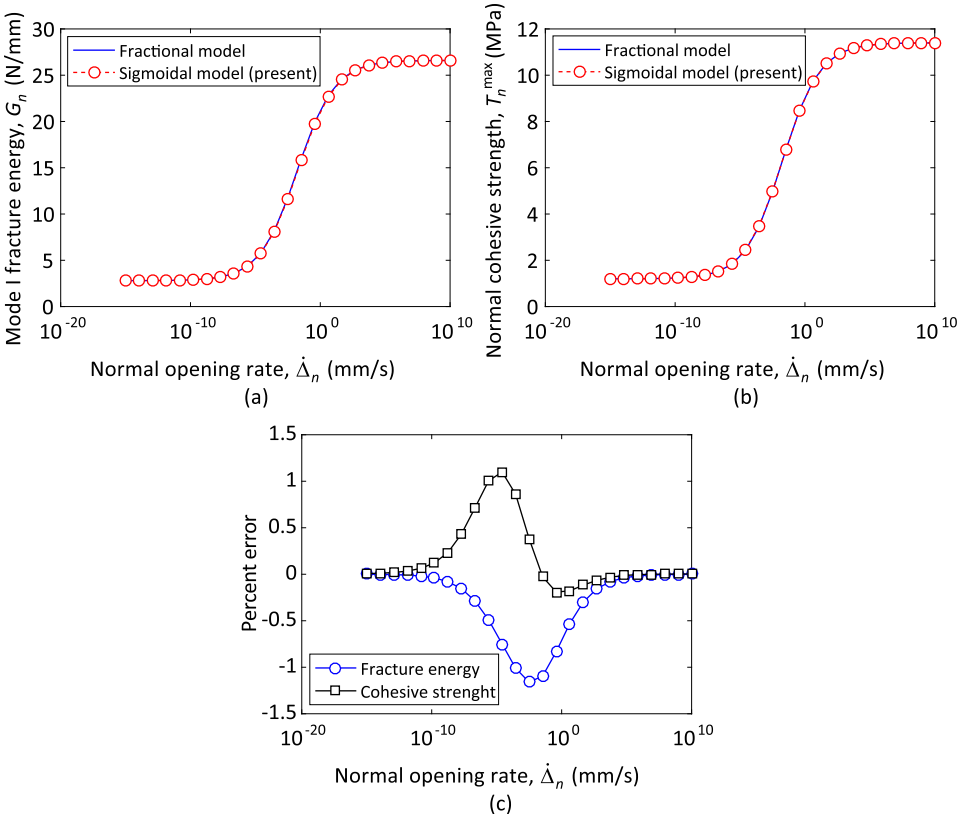

Fig. 3. Mode I fracture energy (a) and cohesive strength (b) obtained from Eqs. (20) and (21), respectively, are compared against those obtained from the fractional viscoelastic CZM [42]. The percent error between the sigmoidal model (present) and the fractional model (c) are below 1.2% for both fracture energy and cohesive strength. The cohesive parameters used for the cohesive model in [42] are: $\phi_n = \phi_t = 2.8$ N/mm, $\sigma_{max} = \tau_{max} = 1.2$ MPa, $\alpha = \beta = 3.5, \lambda_n = \lambda_t = 0.45, \hat{\nu} = 0.3, c = 8.5$, and $\hat{\lambda_n} = \hat{\lambda_t} = 3.5$, while the properties used for the present formulation are: $\phi_n = \phi_t = 2.8$ N/mm, $\sigma_{max} = \tau_{max} = 1.2$ MPa, $\dot{\Delta}_n = \dot{\Delta}_t = 0.0184$ mm/s, $\beta_n = \beta_t = 9.5$, and $p = 0.3$.

Alternatively, Webb and Aigantis [74] associated the non-monotonic fracture energy behavior to the stick-slip phenomenon, which is characterized by sudden changes in crack tip velocities during a fracture test. Due to the sudden changes in crack velocity, Webb and Aigantis [74] include inertial effects in front of the crack via a material inertial shielding term that multiplies the static equilibrium fracture energy. In a study by de Gennes [75], he indicated that the non-monotonous behavior of the fracture energy in a finite viscoelastic specimen was attributed to the viscous dissipation around the crack tip. To explain this, de Gennes [75] divided the region around the crack tip into three zones: an unrelaxed, glassy zone; a viscous dissipation zone; and a fully relaxed, rubbery zone. When the specimen is of infinite size, the volume of the viscous dissipation zone can grow indefinitely (which Hui et al. [76] had previously demonstrated) as the crack speed increases, allowing the fracture energy to increase with crack speed. However, when the size of the specimen is finite, the volume occupied by the viscous dissipation zone is limited, leading to a non-monotonic fracture energy versus crack-opening rate behavior. This behavior was verified computationally by Rahul-Kumar [15].

The observations above can be used to extend the present formulation to model the rate-dependent fracture for both rubbery and glassy polymers. Following the observations by Williams [71] and Johnson and Radon [72], one possible way of extending the present formulation is by incorporating thermomechanical effects in the CZM, allowing for thermal softening of the rate-dependent spring model introduced in Section 2.1. Another possible extension of the present model can be achieved by modifying the damage parameters to be rate-dependent. One way of achieving rate-dependence in the damage parameters follows from a study by Park et al. [77], who used the Schapery correspondence principle [12] to show experimentally that damage depends on both strain and strain rate. Our model can be reformulated by using a suitable version of the Schapery correspondence principle and by prescribing the evolution of damage parameters in terms of *pseudo-crack-openings*. Although such model extension is achievable, it is outside the scope of the present study.

2.4. Material tangent matrix

Implementing the current rate-dependent model within the FE framework requires the derivation of the consistent material tangent matrix. This is achieved by computing the first variation of the cohesive tractions, T_k, from Eq. (19) as follows

$$\delta T_n\left(\Delta_n, \dot{\Delta}_n\right) = \left[\frac{\partial T_n}{\partial \Delta_n} + \frac{\partial T_n}{\partial \dot{\Delta}_n}\frac{\partial \dot{\Delta}_n}{\partial \Delta_n}\right]\delta\Delta_n + \left[\frac{\partial T_n}{\partial \Delta_t} + \frac{\partial T_n}{\partial \dot{\Delta}_t}\frac{\partial \dot{\Delta}_t}{\partial \Delta_t}\right]\delta\Delta_t, \tag{24}$$

and

$$\delta T_t\left(\Delta_n, \dot{\Delta}_n\right) = \left[\frac{\partial T_t}{\partial \Delta_n} + \frac{\partial T_t}{\partial \dot{\Delta}_n}\frac{\partial \dot{\Delta}_n}{\partial \Delta_n}\right]\delta\Delta_n + \left[\frac{\partial T_t}{\partial \Delta_t} + \frac{\partial T_t}{\partial \dot{\Delta}_t}\frac{\partial \dot{\Delta}_t}{\partial \Delta_t}\right]\delta\Delta_t, \tag{25}$$

The material tangent matrix takes the form

$$\mathbf{D}(\Delta_n, \Delta_t) = \begin{bmatrix} D_{tt} & D_{tn} \\ D_{nt} & D_{nn} \end{bmatrix}, \tag{26}$$

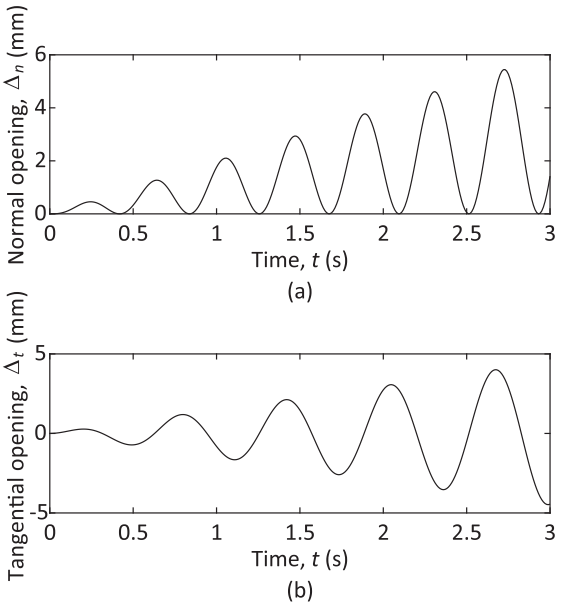

Fig. 4. Normal crack opening (a) and tangential crack opening (b) obtained from Eq. (23).

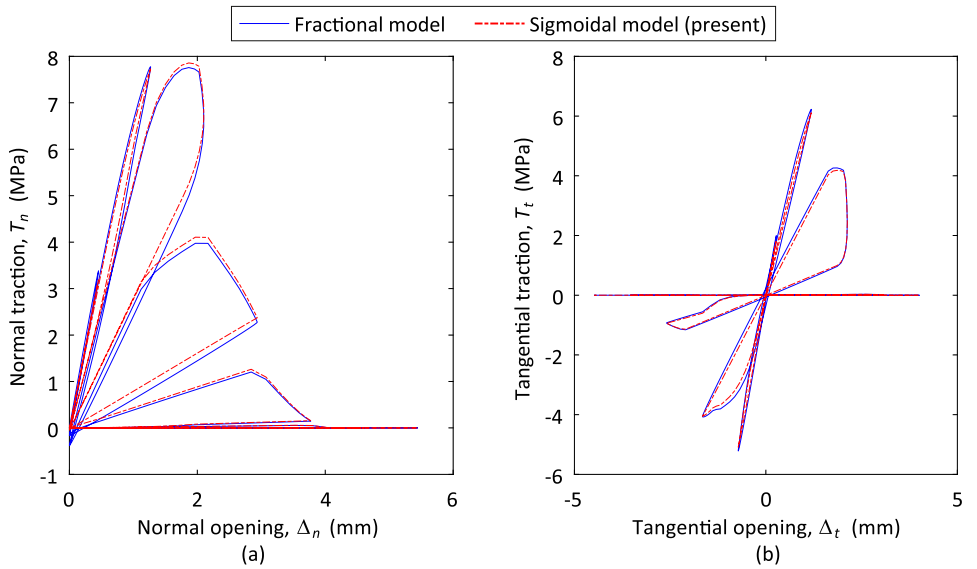

Fig. 5. Rate-dependent cohesive tractions obtained for the general crack opening path given by Eq. (23). The normal cohesive tractions (a) and tangential cohesive tractions (b) obtained from the present formulation correlate well with those obtained from the fractional viscoelastic CZM [42].

where the terms D_{nn} and D_{nt} in Eq. (26) are given by the first and second terms in square brackets from Eq. (24). Similarly, the terms D_{tn} and D_{tt} in Eq. (26) are obtained from the first and second terms in square brackets from Eq. (25). Assuming a backward finite difference approximation for the normal and tangential opening rates, and substituting Eq. (18) into Eqs. (24) and (25) yields:

$$D_{tt} = \frac{S_t}{E_t \kappa_t}\left[\hat{D}_{tt}(\kappa_n,\kappa_t) - \frac{\hat{T}_t(\kappa_n,\kappa_t)}{\kappa_t}\right]\frac{\partial \kappa_t}{\partial \Delta_t} + \frac{\hat{T}_t(\kappa_n,\kappa_t)}{\kappa_t}\left[f_t\left(\left|\dot{\Delta}_t\right|\right) + \dot{\Delta}_t f\prime_t\left(\left|\dot{\Delta}_t\right|\right)\mathrm{sgn}\left(\dot{\Delta}_t\right)\right], \tag{27}$$

$$D_{tn} = \frac{S_t}{E_t \kappa_t}\hat{D}_{tn}(\kappa_n,\kappa_t)\frac{\partial \kappa_n}{\partial \Delta_n}, \tag{28}$$

$$D_{nt} = \frac{S_n}{E_n \kappa_n}\hat{D}_{nt}(\kappa_n,\kappa_t)\frac{\partial \kappa_t}{\partial \Delta_t}, \tag{29}$$

$$D_{nn} = \frac{S_n}{E_n \kappa_n}\left[\hat{D}_{nn}(\kappa_n,\kappa_t) - \frac{\hat{T}_n(\kappa_n,\kappa_t)}{\kappa_n}\right]\frac{\partial \kappa_n}{\partial \Delta_n} + \frac{\hat{T}_n(\kappa_n,\kappa_t)}{\kappa_n}\left[f_n\left(\left|\dot{\Delta}_n\right|\right) + \dot{\Delta}_n f\prime_n\left(\left|\dot{\Delta}_n\right|\right)\mathrm{sgn}\left(\dot{\Delta}_n\right)\right]. \tag{30}$$

The terms $\hat{D}_{tt}, \hat{D}_{tn}, \hat{D}_{nt}$, and $\hat{D}_{nn}$ in Eqs. (27)–(30) are the components of the material tangent matrix from the PPR cohesive zone model [78] evaluated at the kinematic quantities κ_n and κ_t, as shown below:

$$\hat{D}_{tt}(\kappa_n,\kappa_t) = \frac{\Gamma_t}{\delta_t^2}\left[(n^2-n)\left(1-\frac{\kappa_t}{\delta_t}\right)^{\beta}\left(\frac{n}{\beta}+\frac{\kappa_t}{\delta_t}\right)^{n-2} + (\beta^2-\beta)\left(1-\frac{\kappa_t}{\delta_t}\right)^{\beta-2}\left(\frac{n}{\beta}+\frac{\kappa_t}{\delta_t}\right)^{n} - 2\beta n\left(1-\frac{\kappa_t}{\delta_t}\right)^{\beta-1}\left(\frac{n}{\beta}+\frac{\kappa_t}{\delta_t}\right)^{n-1}\right] \times \left[\Gamma_n\left(1-\frac{\kappa_n}{\delta_n}\right)^{\alpha}\left(\frac{m}{\alpha}+\frac{\kappa_n}{\delta_n}\right)^{m} + \langle \phi_n - \phi_t\rangle\right], \tag{31}$$

$$\hat{D}_{tn}(\kappa_n,\kappa_t) = \hat{D}_{nt}(\kappa_n,\kappa_t) = \frac{\Gamma_n\Gamma_t}{\delta_n\delta_t}\left[m\left(1-\frac{\kappa_n}{\delta_n}\right)^{\alpha}\left(\frac{m}{\alpha}+\frac{\kappa_n}{\delta_n}\right)^{m-1} - \alpha\left(1-\frac{\kappa_n}{\delta_n}\right)^{\alpha-1}\left(\frac{m}{\alpha}+\frac{\kappa_n}{\delta_n}\right)^{m}\right] \times \left[n\left(1-\frac{\kappa_t}{\delta_t}\right)^{\beta}\left(\frac{n}{\beta}+\frac{\kappa_t}{\delta_t}\right)^{n-1} - \beta\left(1-\frac{\kappa_t}{\delta_t}\right)^{\beta-1}\left(\frac{n}{\beta}+\frac{\kappa_t}{\delta_t}\right)^{n}\right], \tag{32}$$

$$\hat{D}_{nn}(\kappa_n,\kappa_t) = \frac{\Gamma_n}{\delta_n^2}\left[(m^2-m)\left(1-\frac{\kappa_n}{\delta_n}\right)^{\alpha}\left(\frac{m}{\alpha}+\frac{\kappa_n}{\delta_n}\right)^{m-2} + (\alpha^2-\alpha)\left(1-\frac{\kappa_n}{\delta_n}\right)^{\alpha-2}\left(\frac{m}{\alpha}+\frac{\kappa_n}{\delta_n}\right)^{m} - 2\alpha m\left(1-\frac{\kappa_n}{\delta_n}\right)^{\alpha-1}\left(\frac{m}{\alpha}+\frac{\kappa_n}{\delta_n}\right)^{m-1}\right] \times \left[\Gamma_t\left(1-\frac{\kappa_t}{\delta_t}\right)^{\beta}\left(\frac{n}{\beta}+\frac{\kappa_t}{\delta_t}\right)^{n} + \langle \phi_t - \phi_n\rangle\right]. \tag{33}$$

For further details on the finite element implementation for a two-dimensional linear cohesive element, the interested reader is referred to Ref. [78]. Similarly, the implementation details for three-dimensional cohesive elements can be found in Ref. [79].

Notice that a single set of Eqs. (27)–(30) is used to define all possible loading-unloading-reloading scenarios. All loading scenarios are implicitly defined in terms of the values of $\partial\kappa_n/\partial\Delta_n$ and $\partial\kappa_t/\partial\Delta_t$. For instance, $\partial\kappa_n/\partial\Delta_n = 0$ and $\partial\kappa_n/\partial\Delta_n = 1$ indicate unloading-reloading and loading conditions in the normal direction, respectively. Similarly, $\partial\kappa_t/\partial\Delta_t = 0$ and $\partial\kappa_t/\partial\Delta_t = \Delta_t/|\Delta_t|$ indicate unloading-reloading, and loading conditions in the tangential direction, respectively. The value $\Delta_t/|\Delta_t|$ is used to determine the sign of $\partial\kappa_t/\partial\Delta_t$. These derivatives are obtained from Eq. (17) and are shown below

$$\frac{\partial\kappa_n}{\partial\Delta_n} = \begin{cases} 1 & \text{if } \Delta_n = \kappa_n \\ 0 & \text{if } \Delta_n < \kappa_n \end{cases}, \tag{34}$$

$$\frac{\partial\kappa_t}{\partial\Delta_t} = \begin{cases} \frac{\Delta_t}{|\Delta_t|} & \text{if } |\Delta_t| = \kappa_t \\ 0 & \text{if } |\Delta_t| < \kappa_t \end{cases}. \tag{35}$$

The values of $\partial\kappa_n/\partial\Delta_n$ and $\partial\kappa_t/\partial\Delta_t$ (for positive values of Δ_t) are illustrated in Fig. 6, in which three unloading/reloading scenarios are indicated by the gray regions. For instance, partial unloading/reloading occurs in the light gray regions, while pure unloading/reloading occurs in the dark gray region. The white region constitutes pure loading conditions.

3. Examples and discussion

This section presents and discusses two examples to verify and validate the mixed-mode rate-dependent CZM. The first example compares the results from the present model with experimental results available in the literature [36]. The second example illustrates the ability of the model to simulate mixed-mode rate-dependent delamination problems, where the effects of the input parameters are investigated through a parametric analysis.

3.1. Double cantilever beam test

This example investigates the rate-dependent debonding behavior of a rubber interface through a double cantilever beam (DCB) test. The numerical results obtained from the present model are compared with experimental results available in Ref. [36]. The DCB test geometry consists of two steel arms that are partially bonded with a rubber interface. The steel arms are 200 mm long, 8 mm thick, and 25 mm wide. The geometric configuration and load application points for the DCB test are illustrated in Fig. 7. For each test, the load application points are displaced at a constant rate in the direction indicated by the

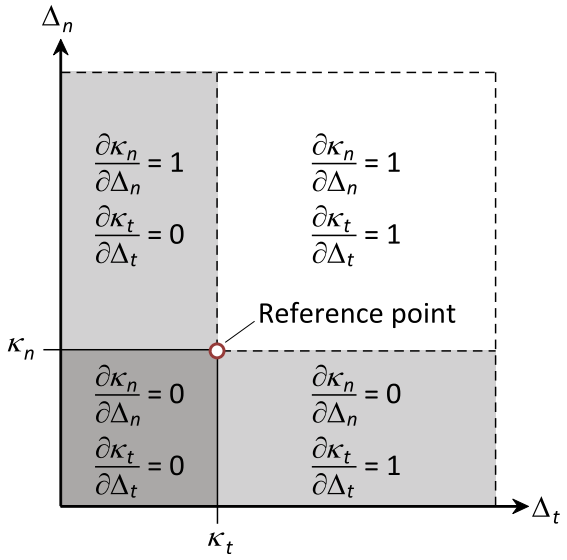

Fig. 6. Given the maximum normal and tangential crack opening during the loading history (reference point), four possible loading scenarios may occur. During pure loading (white region), both $\partial\kappa_n/\partial\Delta_n = 1$ and $\partial\kappa_t/\partial\Delta_t = 1$; if partial unloading conditions occur (light gray regions), $\partial\kappa_n/\partial\Delta_n = 1$ and $\partial\kappa_t/\partial\Delta_t = 0$, when $\Delta_n > \kappa_n$ and $\Delta_t < \kappa_t$, and $\partial\kappa_n/\partial\Delta_n = 0$ and $\partial\kappa_t/\partial\Delta_t = 1$, when $\Delta_n < \kappa_n$ and $\Delta_t > \kappa_t$; and during pure unloading (dark gray region), both $\partial\kappa_n/\partial\Delta_n = 0$ and $\partial\kappa_t/\partial\Delta_t = 0$. This illustration only shows positive values of Δ_t, therefore the values of $\partial\kappa_t/\partial\Delta_t$ shown here need to be multiplied by $\text{sgn}(\Delta_t)$.

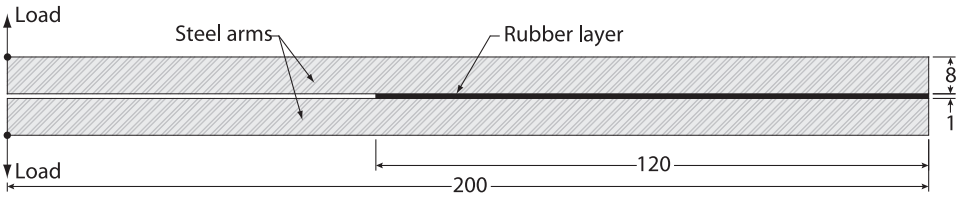

Fig. 7. Geometry and load application points for the double cantilever beam tests (all dimensions are in mm).

arrows on the left end of the beams (see Fig. 7). Several opening rates are used in the tests, (0.01, 0.1, 1, 10, 100, and 500 mm/min), spanning several orders of magnitude.

The steel arms are discretized using 800 bilinear quadrilateral plane strain elements. Each element is 2 mm × 2 mm, as illustrated in Fig. 8. As shown in this figure, we simulated the entire geometry instead of invoking symmetry, which we did for the purposes of this verification and model efficiency study. The material used to model the steel arms is linear elastic, with a Young's modulus of 200 GPa and a Poisson's ratio of 0.3. The rubber interface is discretized using 60 rate-dependent cohesive elements with zero thickness. The cohesive elements are modeled using the rate-dependent cohesive model formulation. A set of fracture parameters that leads to a reasonable agreement between the numerical and experimental results is summarized in Table 1. We determined the values shown in Table 1 by trial an error until the results from our simulations agreed reasonably well with the experimental results from the DCB tests.

From our simulations, we obtain load-displacement curves for each of the opening rates and compare them against those obtained from the experimental DCB tests, as illustrated in Fig. 9. The results show that the applied load predicted by the model approximates well the experimental behavior for opening rates of 1 mm/min or less. However, as the opening rate increases beyond 10 mm/min, the load predicted by our model slightly overestimates that from the experiments. In particular, the peak load predicted by our model overestimates the experimental peak load by about 5% for opening rates of 10 mm/min or more. We believe that some of the difference between our numerical and experimental results is due to the parameters chosen for the cohesive elements (shown in Table 1), which were found by trial and error. An additional source of error is due to the constitutive model that defines the rate-dependent behavior of the cohesive elements, which neglects viscous dissipation.

3.2. Rate-dependent mixed-mode bending test

This example investigates the rate-dependent mixed-mode delamination behavior of a specimen through the mixed-mode bending (MMB) test. The parameters defining the rate-dependent spring (see Section 2.1) are discretely varied within predefined ranges. The results from the rate-dependent model are compared with those from the rate-independent PPR cohesive model [46,78]. The geometry of the MMB test is illustrated in Fig. 10, where $L = 51$ mm, $c = 60$ mm, $h = 1.56$ mm, $B = 25.4$ mm, and $a_0 = 33.7$ mm. The force P, applied on the rigid lever, is evaluated as the reaction force generated after moving point A at a constant speed in a downward direction.

To perform the FE analyses, the bulk domain is discretized using 19,570 bilinear quadrilateral elements, and 683 cohesive elements are inserted along the horizontal direction in front of the notch tip to capture the debonding behavior. The rigid lever is explicitly defined as a rigid element, where constraints to the displacements at points B and C (see Fig. 10) are

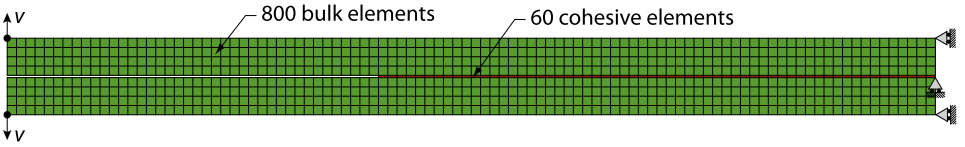

Fig. 8. Finite element mesh and boundary conditions for the double cantilever beam example.

Table 1
Properties of the cohesive elements used to model the rubber interface in the DCB tests.

Mode I and II fracture energies, $\phi_n = \phi_t$ (N/mm)	2.8
Normal and tangential cohesive strengths, $\sigma_{max} = \tau_{max}$ (MPa)	1.2
Non-dimensional shape parameters, $\alpha = \beta$	3.5
Initial slope indicators, $\lambda_n = \lambda_t$	0.45
Exponent of the sigmoidal function, p	0.3
Stiffness indicator parameters, $\beta_n = \beta_t$	9.5
Reference rates, $\dot{\Delta}_{n_0} = \dot{\Delta}_{t_0}$	0.0184

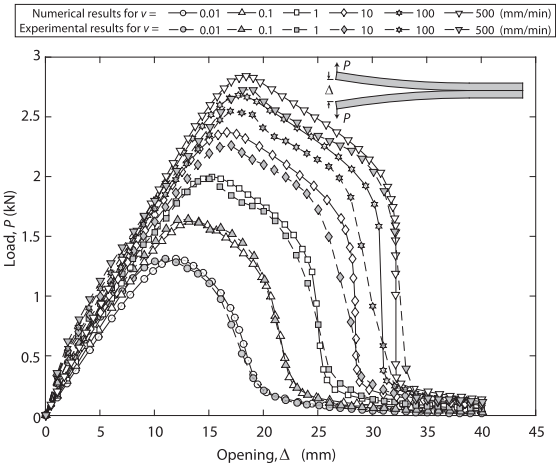

Fig. 9. Load versus Cross-head displacement curves for the double cantilever beam test at different applied opening rates. Experimental results are obtained from Ref. [36].

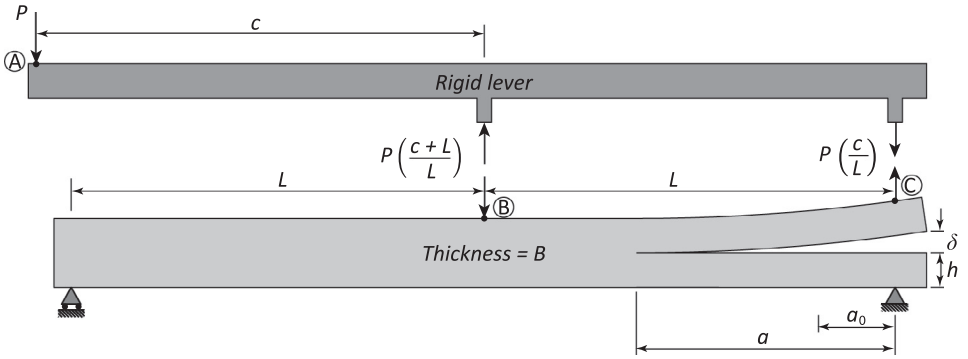

Fig. 10. Geometry and loads for the mixed-mode bending (MMB) test.

imposed to simulate the rigid lever as simply-supported on the beam. The constraints are applied such that points B and C resemble a roller and a pin, respectively. Furthermore, the bulk material is modeled as a linear elastic material with a Young's modulus of 122 GPa and a Poisson's ratio of 0.25, while the cohesive elements are modeled using the rate-dependent formulation described in Section 2. The fracture properties used for the cohesive elements are listed in Table 2. Parameters ϕ_n, ϕ_t, σ_{max}, τ_{max}, α, β, λ_n, and λ_t, which govern the behavior of the damage element, are chosen from Ref. [78], while parameters p, β_n, β_t, $\dot{\Delta}_{n_0}$, and $\dot{\Delta}_{t_0}$, which govern the behavior of the rate-dependent spring model, are arbitrarily chosen to study their effect on the rate-dependent fracture response. To understand the effect of each parameter in the cohesive model on the global response, we vary the values of the fast-to-slow limit stiffness parameters, β_k, the reference rates, $\dot{\Delta}_{k_0}$, and the exponent of the sigmoidal function, p, between predefined values.

Fig. 11 shows the results obtained for different applied displacement rates. We observe that, as the applied displacement rate increases, both the peak force and global fracture energy captured by our rate-dependent cohesive model also increase, which is consistent with the increase in cohesive strength and fracture energy given by Eqs. (20) and (21). In addition, as the applied displacement rate approaches zero the results from the model approach those from the rate-independent PPR cohesive zone model [78].

Fig. 12 shows the results obtained for different fast-to-slow limit stiffness parameters β_k. Note that as the parameter β_k increases, the force P increases. This is because, as β_k increases the rate-dependent spring becomes more sensitive to the crack opening rate. As expected, when $\beta_k = 1$ the result from the rate-independent PPR cohesive zone model is recovered [78]. This is because the rate-dependent model becomes rate-independent after setting $\beta_k = 1$ in Eq. (4). In fact, under these circumstances, the rate-dependent model reduces to the rate-independent version of the PPR cohesive model presented in the study by Spring et al. [45].

The behavior obtained for different reference rates $\dot{\Delta}_{k_0}$ is plotted in Fig. 13. It is observed that as $\dot{\Delta}_{k_0}$ increases, the force P decreases. Moreover, when $\dot{\Delta}_{k_0}$ is large, the response obtained with the rate-dependent model approaches that of the rate-independent one. This behavior can be explained by Eq. (4), where the terms $\dot{\Delta}_k/\dot{\Delta}_{k_0}$ become smaller (for the same applied displacement rate) as $\dot{\Delta}_{k_0}$ increases.

Table 2
Material properties for the rate-dependent cohesive elements used in the MMB tests.

Mode I fracture energy, ϕ_n (N/mm)	0.5
Mode II fracture energy, ϕ_t (N/mm)	1
Normal cohesive strength, $\sigma_{\max}$ (MPa)	20
Tangential cohesive strength, $\tau_{\max}$ (MPa)	100
Non-dimensional shape parameters, $\alpha = \beta$	3
Initial slope indicators, $\lambda_n = \lambda_t$	0.02
Exponent of the sigmoidal function, p	0.1–0.5
Fast-to-slow limit stiffness parameters, $\beta_n = \beta_t$	1–3
Reference rates, $\dot{\Delta}_{n_0} = \dot{\Delta}_{t_0}$ (mm/s)	10^{-3}-10^{2}

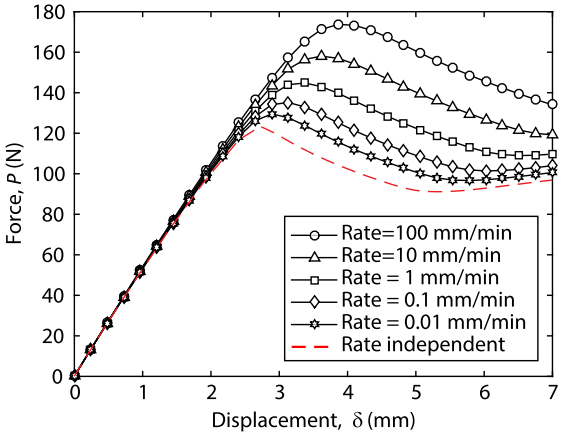

Fig. 11. Effect of the loading rate on the response of the MMB test. The results in this figure are for $\beta_n = \beta_t = 3$, $\dot{\Delta}_{n_0} = \dot{\Delta}_{t_0} = 2 \times 10^{-2}$ mm/s, and $p = 0.3$. As the loading rate decreases, the solution from the present model approaches that of the PPR CZM [46].

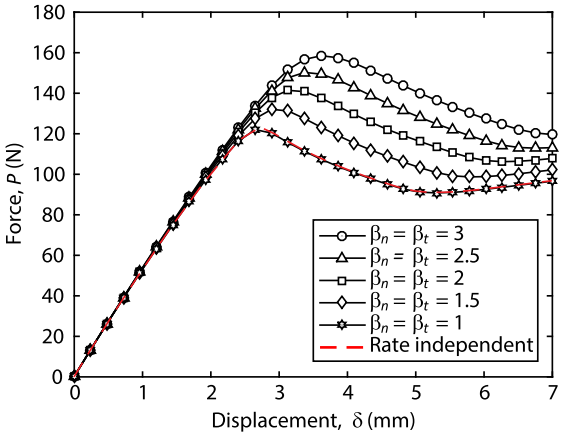

Fig. 12. Effect of the fast-to-slow limit stiffness parameters, β_k, on the response of the MMB test. The results in this figure are for Rate = 10 mm/min, $\dot{\Delta}_{n_0} = \dot{\Delta}_{t_0} = 2 \times 10^{-2}$ mm/s, and $p = 0.3$. As $\beta_k \to 1$ the solution from the present model approaches that of the rate-independent PPR CZM [46].

Finally, the response obtained by varying the exponent p of the sigmoidal expression is plotted in Fig. 14. The results show that, as the parameter p increases, the tractions decrease. This is counterintuitive, because it is expected from Eq. (4) that the transition from slow-limit to fast-limit behavior occurs faster if p is larger. Following this line of thought, it would be expected that a model using a larger value of p is more sensitive to the applied displacement rate, however the opposite is observed from the results. The reason for this unexpected behavior is that for most of the loading history, the crack opening rate in most of the cohesive elements lies below $\dot{\Delta}_{k_0}$. Hence, the terms $\dot{\Delta}_k/\dot{\Delta}_{k_0}$ in Eq. (4) become smaller as p increases.

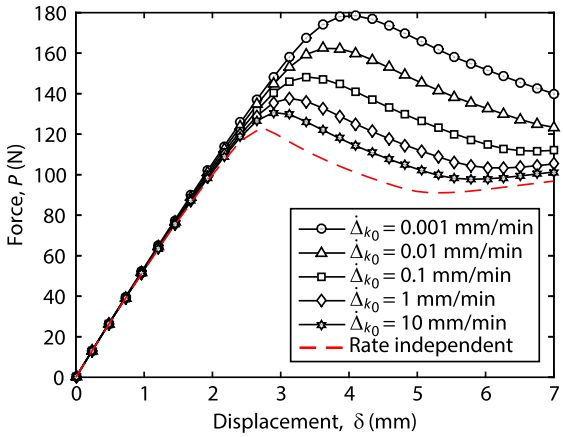

Fig. 13. Effect of the reference rate, $\dot{\Delta}_{k_0}$, on the response of the MMB test. The results in this figure are for Rate = 10 mm/min, $\beta_n = \beta_t = 3$, and $p = 0.3$. As $\dot{\Delta}_{k_0}$ increases, the effects of the loading rate vanish, and it is expected that as $\dot{\Delta}_{k_0} \to \infty$ the solution from the present model approaches that of the rate-independent PPR CZM [46].

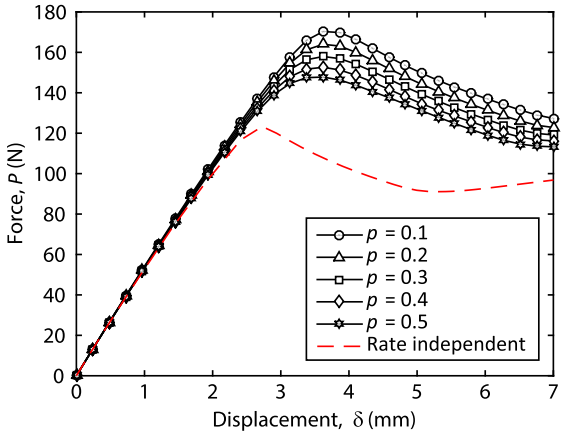

Fig. 14. Effect of the exponent, p, on the response of the MMB test. The results in this figure are for Rate = 10 mm/min, $\dot{\Delta}_{n_0} = \dot{\Delta}_{t_0} = 2 \times 10^{-2}$ mm/s, and $\beta_n = \beta_t = 3$.

4. Computational cost analysis

This section evaluates the computational efficiency of the rate-dependent cohesive model presented in this study. First, we analyze the computational cost for the rate-dependent DCB example of Section 3.1. Next, we analyze the computational cost for the MMB test of Section 3.2. Finally, we go in more depth and study the efficiency of the proposed model using a simplified three-point bending test.

4.1. Double cantilever beam test example

For the double cantilever beam test in Section 3.1, the average CPU time spent in the analysis is 15.2 s for the first four opening rates (i.e., for $v = 0.01$, 0.1, 1, and 10 mm/min), and 20.0 s for the last two opening rates (i.e., for $v = 10$ and 100 mm/min). The last two opening rates took longer, due to the large nonlinear behavior, as observed in Fig. 9. The same models were studied in Ref. [42] using the fractional viscoelastic model discussed in Appendix A. In their study, the average CPU time was 117.7 s for the first four opening rates and 125.6 s for the last two opening rates. Notice that the computational cost using the cohesive model in [42] is 7.7 times greater for the first four opening rates and 4.5 times greater for the last two opening rates. The reason being that the cost per iteration is larger for the model in [42] than it is for the present model (sigmoidal), as will be discussed in detail later.

A better comparison between the present rate-dependent model and the fractional model in Ref. [42] is obtained for each case by normalizing the total CPU time by the number of Newton-Raphson iterations. This leads to an average CPU time per Newton-Raphson iteration of about 0.1 and 0.2 s for the present model (sigmoidal) and the fractional model [42], respectively. Comparing these two values, we can determine that, for this example, the cost per iteration for the fractional model is about 2 times higher than that for the present model.

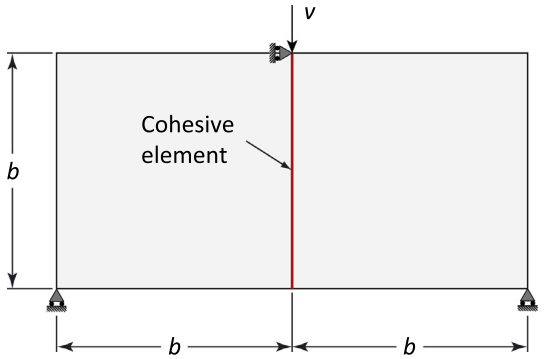

Fig. 15. Simplified three-point bending model geometry used for the computational cost analysis.

Table 3
Properties of the rate-dependent cohesive elements used in the computational cost analysis.

Parameters for damage element (both models)	Mode I and II fracture energies, $\phi_n = \phi_t$ (N/mm)	0.8
	Normal cohesive strength, $\sigma_{max} = \tau_{max}$ (MPa)	10
	Non-dimensional shape parameters, $\alpha = \beta$	3.5
	Initial slope indicators, $\lambda_n = \lambda_t$	0.15
Parameters for rate-dependent spring (sigmoidal model)	Exponent of the sigmoidal function, p	0.3
	Fast-to-slow limit stiffness parameters, $\beta_n = \beta_t$	9.5
	Reference rates, $\dot{\Delta}_{n_0} = \dot{\Delta}_{t_0}$ (mm/s)	0.015
Parameters for springpot (fractional model [42])	Order of the fractional derivative, $\hat{v}$	0.3
	Stiffness parameter, c	8.5
	Springpot viscosity parameters, $\hat{\lambda} = \hat{\eta}_n/(cE_n) = \hat{\eta}_t/(cE_t)$	3.5

4.2. Mixed-mode bending test example

For the mixed-mode bending test in Section 3.2, the average CPU time required to run these models is 14.2 min. After normalizing the computational time with respect to the total number of Newton-Raphson iterations required by each model, the average CPU time per Newton-Raphson iteration for all the models in this example is about 2 s. This average CPU time per iteration is slightly larger than that of the thermodynamically consistent PPR model [45], which reported less than 2 s. Based on these results, we found that the present rate-dependent model requires approximately 16% more CPU time per iteration than the rate-independent PPR model in [45].

4.3. Simplified three-point bending test

Here, the computational efficiency is assessed by determining the cost per Newton-Raphson iteration for the simplified three-point bending model illustrated in Fig. 15. This simple model consists of two four-node plane strain quadrilateral elements of dimension $b = 1$ m, connected by a rate-dependent cohesive element. The nodes at the top center of the model are moved vertically at a constant speed $v = 1$ mm/s in the direction indicated by the arrow, until a deflection of $0.1b$ is reached. The FE model shown in Fig. 15 resembles a three-point bending test that allows us, without loss of generality, to assess the computational efficiency of the present rate-dependent CZM. The efficiency of the present model is compared with that of the fractional CZM presented in Ref. [42] (see Appendix A). The computational costs in this section were obtained from a Matlab implementation of both the present (sigmoidal) model and the fractional model in Ref. [42].

The properties used for the cohesive element in Fig. 15, for both the sigmoidal model (present formulation) and the fractional model [42], are shown in Table 3. The bulk elements in Fig. 15 are modeled as linear elastic with a Young's modulus of $E = 70$ GPa and a Poisson's ratio $\nu = 0.25$.

Fig. 16 shows the average computational cost per Newton-Raphson iteration for an increasing number of load steps, for both the sigmoidal model (present formulation) and the fractional cohesive model of Ref. [42]. The average computational time for a given number of load steps is depicted as the average of four separate analyses. For each analysis, the computational cost corresponds to the time per Newton-Raphson iteration spent by each model to assemble the stiffness matrix and the load vector for the cohesive element only. The computational analysis was conducted on a computer with an Intel(R) Core(TM) i7-6600U CPU 2.60 GHz processor and 20 GB installed RAM memory.

The results illustrated in Fig. 16 show that the computational cost per iteration for the sigmoidal model is approximately equal to 8×10^{-4} s, and is practically independent of the number of load steps used. However, this is not the case for the fractional model, in which the computational cost increases exponentially as the number of load steps increases. The reason

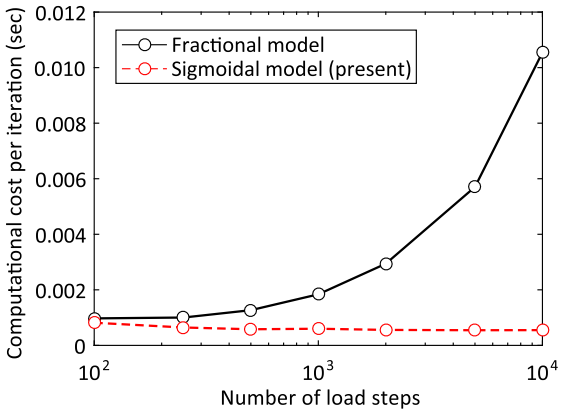

Fig. 16. Average computational cost per Newton-Raphson iteration obtained for a three-point bending test consisting of two four-node plane strain quadrilateral elements bonded by either the present rate-dependent cohesive element or the fractional viscoelastic cohesive element of Ref. [42]. The average computational times are obtained using a computer with an Intel(R) Core(TM) i7-6600U CPU 2.60 GHz processor and 20 GB installed RAM memory.

for this increase is that, in order to find the viscoelastic traction at each load step the fractional model [42] needs to compute an integral over all previous time increments, as indicated by Eqs. (36) and (37).

The fact that the computational cost per iteration for the present formulation is always smaller than the computational cost for the fractional CZM [42], highlights the gain in computational cost achieved with the present CZM. The savings in computational cost is much higher as the number of cohesive elements increase, not only because the cost of computing the integrals in Eqs. (36) and (37) is avoided, but also because there are significant savings in storage due to the fact that one need not store the entire history of tractions and displacements at each Gauss point for each cohesive element, as is the case in the fractional model presented in Ref. [42].

5. Summary and conclusions

This study presents an efficient mixed-mode rate-dependent cohesive fracture model that approximates the behavior of fractional viscoelastic models using two rate-dependent springs, aligned perpendicular and parallel to the crack plane, to account for fracture in modes I and II, respectively. The traction-separation relation for each spring is forced to be continuous with respect to changes in the crack opening rates, resembling the behavior of viscoelastic materials. The proposed cohesive model is framed in the context of damage mechanics, where two scalar damage parameters are used to scale the undamaged tractions obtained from the rate-dependent spring models. The scalar damage parameters are consistent with the PPR cohesive fracture model [46] and take the form developed by Spring et al. [45]. The evolution laws for the damage parameters are such that they satisfy the second law of thermodynamics.

The simplified formulation in this study demonstrated a level of accuracy that can be compared to that from a more sophisticated fracture model such as that presented in Ref. [42]. Moreover, the results from this investigation show that the present formulation is computationally more efficient and demonstrates savings in computational cost that can reach an order of magnitude compared to the fractional model in Ref. [42]. Specifically, the savings in computational cost were more pronounced as the number of load steps increased. The present model is computationally more efficient, because it is formulated in such a way that the undamaged tractions from the rate-dependent springs can be obtained without computing convolution integrals involving the entire history of crack opening displacements and tractions, as is the case of the fractional model [42].

The present model can open new avenues to simulate rate-dependent crack propagation problems in an efficient manner, while maintaining a similar level of accuracy as that of more sophisticated models. However, we recognize that the model has room for improvement. For example, the stiffness of the rate-dependent springs could be enhanced by additional internal state variables to account for viscous dissipation [80]. Moreover, the present formulation can be extended to a cohesive-frictional model using, for example, some ideas from the studies by Ruina [81], Serpieri et al. [82], Parrinello et al. [83,84], and Spring and Paulino [85,86]. Finally, to model the fracture behavior of glassy polymers, the model can be enhanced to include thermo-mechanical effects based upon the work by Williams [71] or reformulated in terms of a pseudo-energy functional, following the study by Park et al. [77].

Acknowledgments

The authors gratefully acknowledge support by the Raymond Allen Jones Chair at the Georgia Institute of Technology. The authors would also like to extend their appreciation to Dr. Lauren Lukkarila for her advice and input to this publication. The

information presented in this paper is the sole opinion of the authors and does not necessarily reflect the views of the sponsors or sponsoring agencies.

Appendix A. Rate-dependent cohesive zone model based on fractional viscoelasticity [42]

The rate-dependent CZM presented in Ref. [42] uses a viscoelastic model based on a fractional standard linear solid (SLS) model in series with a damage element that is compatible with the PPR CZM [45] (see Section 2.2). A rheological representation of the fractional SLS used in Ref. [42] is illustrated in Fig. 17. Each of the diamond-shaped elements in Fig. 17 is referred to as a *springpot*. A springpot is an element that is more general than a spring or a dashpot and whose constitutive equation uses a differential operator of fractional order, $D_t^{\hat{v}}(\cdot)$, as follows:

$$\sigma_k(t) = \hat{\eta}_k D_t^{\hat{v}} \delta_k(t), \tag{36}$$

where

$$D_t^{\hat{v}} \delta_k(t) = \frac{1}{\Gamma(1-\hat{v})} \int_0^t \frac{\dot{\delta}_k(\tau)}{(t-\tau)^{\hat{v}}}, \quad 0 < \hat{v} < 1 \tag{37}$$

is the Caputo fractional derivative of order $\hat{v} \in (0,1)$ [41]. Parameters $\hat{\eta}_k$ are viscosity-like parameters, and $\delta_k(t)$ are the deformations of the springpot in the normal ($k = n$) and tangential ($k = t$) directions, respectively. A constitutive relationship similar to that in Eq. (36) was proposed in 1947 by Scott-Blair [87] to represent a material that behaves between a Hookean solid and a Newtonian fluid. Because Eq. (36) is defined in terms of a fractional differential operator of order $\hat{v} \in (0,1)$, a material governed by this constitutive relation will behave as a spring if $\hat{v} \to 0$ or as a dashpot if $\hat{v} \to 1$.

The normal and tangential cohesive tractions derived in [42] are computed as

$$T_k = (1 - d_k) S_k, \quad (k = n,\ t), \tag{38}$$

where d_k are damage parameters obtained from the PPR cohesive zone model [46], cf. Eq. (5), and S_k are undamaged cohesive tractions obtained from the solution of the fractional differential equations

$$S_k + \hat{\lambda}_{k0} D_t^{\hat{v}} S_k = E_k \Delta_k + \hat{\gamma}_{k0} D_t^{\hat{v}} \Delta_k, \quad (k = n, t), \tag{39}$$

where

$$\hat{\lambda}_k = \hat{\eta}_k / (cE_k), \quad \text{and} \quad \hat{\gamma}_k = \hat{\eta}_k (1 + c)/c. \tag{40}$$

The fractional differential Eqs. (39) govern the response of each of the fractional standard SLS models in Fig. 17 (neglecting the damage elements). The derivation of the fractional differential equations for a fractional SLS model is standard, and can be obtained using a similar procedure as that used to obtain the differential equation for a SLS model that uses a dashpot instead of a springpot [e.g., see 41].

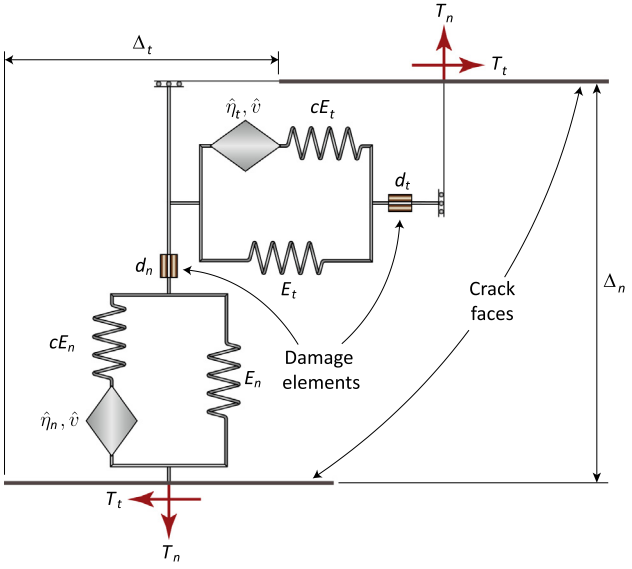

Fig. 17. Mixed-mode rate-dependent CZM based on a fractional standard linear solid model as presented in Ref. [42].

To calculate the undamaged tractions, S_k, one must solve the fractional differential Eqs. (39) numerically. In order to do so, the Caputo fractional derivatives are approximated. The Caputo fractional derivative at time $t = t_N$ of a given function $f(t)$ is approximated as

$$ {}_0D_t^{\hat{\nu}} f(t_N) = \frac{1}{\Gamma(1-\hat{\nu})} \int_0^{t_N} \frac{\dot{f}(\tau)}{(t_N-\tau)^{\hat{\nu}}} \mathrm{d}\tau \approx \frac{1}{\Gamma(1-\hat{\nu})} \sum_{j=1}^{N} \frac{f(t_j)-f(t_{j-1})}{t_j - t_{j-1}} \int_{t_{j-1}}^{t_j} (t_N-\tau)^{-\hat{\nu}} \mathrm{d}\tau. \tag{41} $$

The Caputo fractional derivative approximation on the right hand side of Eq. (41) is achieved by replacing the integral on the left hand side by a sum of piecewise integrals, each evaluated on a time interval $(t_{j-1},\ t_j)$, $j = 1, \ldots, N$. In each of the time intervals, the value of $\dot{f}(\tau)$ is replaced by its backward finite difference approximation. Using the approximate Caputo derivative (41) to approximate the fractional derivatives of both tractions S_k and crack opening displacements Δ_k in Eq. (39) yields

$$ S_k(t_N) = \hat{E}_k \Delta_k + \Delta S_k^H, (k = n, t), \tag{42} $$

where

$$ \hat{E}_k = \left(1 + \frac{c\hat{\lambda}_k}{\hat{\lambda}_k + \Gamma(2-\hat{\nu})\Delta t_N^{\hat{\nu}}}\right) E_k, \quad \Delta S_k^H = \frac{\hat{\lambda}_k S_{S_k} - \hat{\gamma}_k S_{\Delta_k}}{\hat{\lambda}_k + \Gamma(2-\hat{\nu})\Delta t_N^{\hat{\nu}}}, \tag{43} $$

and

$$ \begin{aligned} S_{S_k} &= S_k(t_{N-1}) + \sum_{j=1}^{N-1} [S_k(t_j) - S_k(t_{j-1})] A_j, \\ S_{\Delta_k} &= \Delta_k(t_{N-1}) + \sum_{j=1}^{N-1} [\Delta_k(t_j) - \Delta_k(t_{j-1})] A_j. \end{aligned} \tag{44} $$

The terms ΔS_k^H in Eq. (42) are interpreted as history variables because they account for the history of previous stresses and crack opening displacements up to time $t = t_{N-1}$. The rate-dependent cohesive tractions, as presented in Ref. [42], are obtained after substituting Eqs. (5) and (42) into Eq. (38), yielding

$$ T_k = \frac{\hat{T}_k(\kappa_n, \kappa_t)}{E_k \kappa_k} \left(\hat{E}_k \Delta_k + \Delta S_k^H\right), \quad (k = n, t). \tag{45} $$

Appendix B. Nomenclature

α	parameter controlling the shape of the cohesive softening curve in the normal direction
$\bar{\delta}_n$	conjugate normal final crack opening width
$\bar{\delta}_t$	conjugate tangential final crack opening width
β	parameter controlling the shape of the cohesive softening curve in the tangential direction
β_n	fast-to-slow limit stiffness ratio in the normal direction
β_t	fast-to-slow limit stiffness ratio in the tangential direction
δ_{nc}	normal crack opening width at the peak normal traction in the original PPR model
Δ_n	normal separation along the fracture surface
δ_n	normal final crack opening width
Δ_n^{N+1}	normal separation along the fracture surface at time increment $N+1$
Δ_n^N	normal separation along the fracture surface at time increment N
δ_{tc}	tangential crack opening width at the peak normal traction in the original PPR model
Δ_t	tangential separation along the fracture surface
δ_t	tangential final crack opening width
Δ_t^{N+1}	tangential separation along the fracture surface at time increment $N+1$
Δ_t^N	tangential separation along the fracture surface at time increment N
$\dot{\Delta}_{n_0}$	normal reference separation rate for the rate-dependent spring model
$\dot{\Delta}_{t_0}$	tangential reference separation rate for the rate-dependent spring model
Γ_n	energy constant in the PPR model
Γ_t	energy constant in the PPR model
$\hat{D}_{nn}, \hat{D}_{nt}$	normal components of the material tangent stiffness matrix from the original PPR model
$\hat{D}_{tn}, \hat{D}_{tt}$	tangential components of the material tangent stiffness matrix from the original PPR model

$\hat{T}_n$	normal cohesive traction in the original PPR model
$\hat{T}_t$	tangential cohesive traction in the original PPR model
κ_n	kinematic quantity defining the maximum normal crack opening width in the history of loading
κ_n^{N+1}	maximum normal crack opening width at time increment $N+1$
κ_n^{N}	maximum normal crack opening width at time increment N
κ_t	kinematic quantity defining the maximum absolute tangential crack opening width in the history of loading
κ_t^{N+1}	maximum absolute tangential crack opening width at time increment $N+1$
κ_t^{N}	maximum absolute tangential crack opening width at time increment N
λ_n	parameter controlling the hardening slope of the PPR model in the normal direction
λ_t	parameter controlling the hardening slope of the PPR model in the normal direction
$(\cdot)$	time derivative
$\langle\cdot\rangle$	Macauley bracket
$\mathbf{D}$	material tangent stiffness matrix
ϕ_n	fracture energy in the normal direction (with zero tangential separation)
ϕ_t	fracture energy in the tangential direction (with zero tangential separation)
$\sigma_{\max}$	cohesive strength in the normal direction from the original PPR model
$\tau_{\max}$	cohesive strength in the tangential direction from the original PPR model
$\tilde{E}_n$	stiffness of the rate-dependent spring model in the normal direction
$\tilde{E}_t$	stiffness of the rate-dependent spring model in the tangential direction
D_{nn}, D_{nt}	normal components of the material tangent stiffness matrix for the rate-dependent CZM
d_n	normal scalar damage parameter consistent with the PPR model
D_{tn}, D_{tt}	tangential components of the material tangent stiffness matrix for the rate-dependent CZM
d_t	tangential scalar damage parameter consistent with the PPR model
E_n	initial stiffness parameter for the PPR model in the normal direction
E_t	initial stiffness parameter for the PPR model in the tangential direction
G_n	rate-dependent fracture energy in the normal direction
G_t	rate-dependent fracture energy in the tangential direction
m	nondimensional exponent in the PPR model
n	nondimensional exponent in the PPR model
p	exponent of the sigmoidal function for the rate-dependent spring model
S_n	normal undamaged traction from rate-dependent spring model
S_t	tangential undamaged traction from rate-dependent spring model
T_n	rate-dependent cohesive traction in the normal direction
$T_n^{\max}$	rate-dependent cohesive strength in the normal direction
T_t	rate-dependent cohesive traction in the tangential direction
$T_t^{\max}$	rate-dependent cohesive strength in the tangential direction

References

[1] Schapery RA. Application of thermodynamics to thermomechanical, fracture, and birefringent phenomena in viscoelastic media. J Appl Phys 1964;35(5):1451–65.
[2] Williams ML. Initiation and growth of viscoelastic fracture. Tech. rep. NASA; 1965.
[3] Wnuk MP, Knauss WG. Delayed fracture in viscoelastic-plastic solids. Int J Solids Struct 1970;6(7):995–1009.
[4] Mueller HK, Knauss WG. Crack propagation in a linearly viscoelastic strip. J Appl Mech 1971;38(2):483–8.
[5] Schapery RA. A theory of crack initiation and growth in viscoelastic media. I. Theoretical development. Int J Fract 1975;11(1):141–59.
[6] Schapery RA. A theory of crack initiation and growth in viscoelastic media. I. Approximate methods of analysis. Int J Fract 1975;11(3):369–88.
[7] Schapery RA. A theory of crack initiation and growth in viscoelastic media. I. Analysis of continuous growth. Int J Fract 1975;11(4):549–62.
[8] Dugdale DS. Yielding of steel sheets containing slits. J Mech Phys Solids 1960;8(2):100–4.
[9] Barenblatt GI. The mathematical theory of equilibrium cracks in brittle fracture. Adv Appl Mech 1962;7:55–129.
[10] Knauss WG. Delayed failure — the Griffith problem for linearly viscoelastic materials. Int J Fract Mech 1970;6(1):7–20.
[11] Knauss WG, Dietmann H. Crack propagation under variable load histories in linearly viscoelastic solids. Int J Eng Sci 1971;8(8):643–56.
[12] Schapery RA. Correspondence principles and a generalized J integral for large deformation and fracture analysis of viscoelastic media. Int J Fract 1984;25(3):195–223.
[13] Rice JR. A path independent integral and the approximate analysis of strain concentration by notches and cracks. J Appl Mech 1968:379–86.
[14] Rahul-Kumar P, Jagota A, Bennison SJ, Saigal S, Muralidhar S. Polymer interfacial fracture simulations using cohesive elements. Acta Mater 1999;47(15–16):4161–9.
[15] Rahul-Kumar P, Jagota A, Bennison SJ, Saigal S. Cohesive element modeling of viscoelastic fracture: application to peel testing of polymers. Int J Solids Struct 2000;37:1873–97.
[16] Zhou F, Molinari JF, Shioya T. A rate-dependent cohesive model for simulating dynamic crack propagation in brittle materials. Eng Fract Mech 2005;72:1383–410.
[17] Makhecha DP, Kapania RK, Johnson ER, Dillard DA, Jacob GC, Starbuck M. Rate-dependent cohesive zone modeling of unstable crack growth in an epoxy adhesive. Mech Adv Mater Struct 2009;16(1):12–9.

[18] Marzi S, Hesebeck O, Brede M, Kleiner F. A rate-dependent cohesive zone model for adhesively bonded joints loaded in mode I. J Adhes Sci Technol 2009;23:881–98.
[19] Musto M, Alfano G. A novel rate-dependent cohesive-zone model combining damage and visco-elasticity. Comput Struct 2013;118:126–33.
[20] May M, Hesebeck O, Marzi S, Böhme W, Lienhard J, Kilchert S, et al. Rate dependent behavior of crash-optimized adhesives – experimental characterization, model development, and simulation. Eng Fract Mech 2015;133:112–37.
[21] Kim YR, Allen DH, Little DN. Damage-induced modeling of asphalt mixtures through computational micromechanics and cohesive zone fracture. Mater Civ Eng 2005;17:477–84.
[22] Kim YR, Allen DH, Little DN. Computational constitutive model for predicting nonlinear viscoelastic damage and fracture failure of asphalt concrete mixtures. Int J Geomech 2007;7(2):102–10.
[23] Kim YR, Aragão FTS. Microstructure modeling of rate-dependent fracture behavior in bituminous paving mixtures. Finite Elem Anal Des 2013;63:23–32.
[24] Rosa AL, Yu RC, Ruiz G, Saucedo L, Sousa JLAO. A loading rate dependent cohesive model for concrete fracture. Eng Fract Mech 2012;82:195–208.
[25] Xu XP, Needleman A. Void nucleation by inclusion debonding in a crystal matrix. Modell Simul Mater Sci Eng 1993;1(2):111–32.
[26] Corigliano A, Mariani S, Pandolfi A. Numerical modeling of rate-dependent debonding processes in composites. Compos Struct 2003;61:39–50.
[27] Corigliano A, Mariani S, Pandolfi A. Numerical analysis of rate-dependent dynamic composite delamination. Compos Sci Technol 2006;66:766–75.
[28] Anvari M, Scheider I, Thaulow C. Simulation of dynamic ductile crack growth using strain-rate and triaxiality-dependent cohesive elements. Eng Fract Mech 2006;73:2210–28.
[29] Kazerani T, Zhao GF, Zhao J. Dynamic fracturing simulation of brittle material using the distinct lattice spring method with a full rate-dependent cohesive law. Rock Mech Rock Eng 2010;43(6):717–26.
[30] Valoroso N, Debruyne G, Laverne J. A cohesive zone model with rate-sensitivity for fast crack propagation. Mech Res Commun 2014;58:82–7.
[31] May M, Hesebeck O. Assessment of experimental methods for calibrating rate-dependent cohesive zone models for predicting failure in adhesively bonded metallic structures. Eng Fail Anal 2015;56:441–53.
[32] Gozluklu B, Coker D. Modeling of dynamic crack propagation using rate dependent interface model. Theoret Appl Fract Mech 2016;85:191–206.
[33] Allen DH, Searcy CR. A micromechanical model for a viscoelastic cohesive zone. Int J Fract 2001;107:159–76.
[34] Xu C, Siegmund T, Ramani K. Rate-dependent crack growth in adhesives I. Modeling approach. Int J Adhes Adhes 2003;23:9–13.
[35] Xu C, Siegmund T, Ramani K. Rate-dependent crack growth in adhesives II. Experiments and analysis. Int J Adhes Adhes 2003;23:15–22.
[36] Musto M, Alfano G. A fractional rate-dependent cohesive-zone model. Int J Numer Meth Eng 2015;103(5):313–41.
[37] Zhou W, Tang L, Liu X, Ma G, Chen M. Mesoscopic simulation of the dynamic tensile behaviour of concrete based on a rate-dependent cohesive model. Int J Impact Eng 2016;95:165–75.
[38] Bažant ZP, Li YN. Cohesive crack with rate-dependent opening and viscoelasticity: I. Mathematical model and scaling. Int J Fract 1997;86:247–65.
[39] Li YN, Bažant Z. Cohesive crack model with rate-dependent opening and viscoelasticity: II. Numerical algorithm, behavior and size effect. Int J Fract 1997;86:267–88.
[40] Nguyen TD, Govindjee S, Klein PA, Gao H. A rate-dependent cohesive continuum model for the study of crack dynamics. Comput Methods Appl Mech Eng 2004;193:3239–65.
[41] Mainardi F. Fractional Calculus and Waves in Linear Viscoelasticity. Imperial College Press; 2010.
[42] Giraldo-Londoño O, Paulino GH, Buttlar WG. Fractional calculus derivation of a rate-dependent PPR-based cohesive fracture model: Theory, implementation, and numerical results (submitted for publication).
[43] Volokh KY. Comparison between cohesive zone models. Commun Numer Methods Eng 2004;20(11):845–56.
[44] Alfano G. On the influence of the shape of the interface law on the application of cohesive-zone models. Compos Sci Technol 2006;66(6):723–30.
[45] Spring DW, Giraldo-Londoño O, Paulino GH. A study on the thermodynamic consistency of the Park-Paulino-Roesler (PPR) cohesive fracture model. Mech Res Commun 2016(Part B):100–9.
[46] Park K, Paulino GH, Roesler JR. A unified potential-based cohesive model for mixed-mode fracture. J Mech Phys Solids 2009;57:891–908.
[47] Park K. Potential-based fracture mechanics using cohesive zone and virtual internal bond modeling [Ph.D. thesis]. University of Illinois at Urbana-Champaign; 2009.
[48] Diethelm K, Ford NJ, Freed AD. A predictor-corrector approach for the numerical solution of fractional differential equations. Nonlinear Dyn 2002;29:3–22.
[49] Diethelm K, Ford NJ, Freed AD, Luchko Y. Algorithms for the fractional calculus: a selection of numerical methods. Comput Methods Appl Mech Eng 2005;194:743–73.
[50] Murio DA. On the stable numerical evaluation of Caputo fractional derivatives. Comput Math Appl 2006;51:1539–50.
[51] Li Y, Sun N. Numerical solution of fractional differential equations using the generalized block pulse operational matrix. Comput Math Appl 2011;62:1046–54.
[52] Akgül A, Inc M, Karatas E, Baleanu D. Numerical solutions of fractional differential equations of Lane-Emden type by an accurate technique. Adv Differ Eq 2015;220:1–12.
[53] Krishnasamy VS, Mashayekhi S, Razzaghi M. Numerical solutions of fractional differential equations by using fractional Taylor basis. IEEE/CAA J Autom Sin 2017;4(1):98–106.
[54] Li L, amd Liu Z, Dehghan S, Chen YQ, Xue D. A review and evaluation of numerical tools for fractional calculus and fractional order controls. Int J Control 2017;90(6):1165–81.
[55] Cazes F, Coret M, Combescure A, Gravouil A. A thermodynamic method for the construction of a cohesive law from a nonlocal damage model. Int J Solids Struct 2009;46:1476–90.
[56] Dimitri R, Trullo M, De Lorenzis L, Zavarise G. A consistency assessment of coupled cohesive zone models for mixed-mode debonding problems. Fract Struct Integr 2014;29:266–83.
[57] McGarry JP, Máirtin ÉÓ, Beltz GE. Potential-based and non-potential-based cohesive zone formulations under mixed-mode separation and over-closure. Part I: theoretical analysis. J Mech Phys Solids 2014;63:336–62.
[58] Máirtin ÉÓ, Parry G, Beltz GE, McGarry JP, et al. Potential-based and non-potential-based cohesive zone formulations under mixed-mode separation and over-closure. Part II: finite element applications. J Mech Phys Solids 2014;63:363–85.
[59] Mosler J, Scheider I. A thermodynamically and variationally consistent class of damage-type cohesive models. J Mech Phys Solids 2011;59:1647–68.
[60] Lemaitre J. A Course on Damage Mechanics. Berlin: Springer-Verlag; 1992.
[61] Belytschko T, Liu W, Moran B. Nonlinear Finite Elements for Continua and Structures. John Wiley & Sons, Inc.; 2000.
[62] Al-Rub RKA, Darabi MK, Little DN, Masad EA. A micro-damage healing model that improves prediction of fatigue life in asphalt mixes. Int J Eng Sci 2010;48(11):966–90.
[63] Lee HJ, Kim YR. Viscoelastic continuum damage model of asphalt concrete with healing. J Eng Mech 1998;124(11):1224–32.
[64] Si Z, Little DN, Lytton RL. Characterization of microdamage and healing of asphalt concrete mixtures. J Mater Civ Eng 2002;14(6):461–70.
[65] Brown EN, Sottos NR, White SR. Fracture testing of a self-healing polymer composite. Exp Mech 2002;42(4):372–9.
[66] Toohey KS, Sottos NR, Lewis JA, Moore JS, White SR. Self-healing materials with microvascular networks. Nat Mater 2007;6(8):581–5.
[67] Blaiszik BJ, Kramer SL, Olugebefola SC, Moore JS, Sottos NR, White SR. Self-healing polymers and composites. Annu Rev Mater Res 2010;40:179–211.
[68] Hager MD, Greil P, Leyens C, van der Zwaag S, Schubert US. Self-healing materials. Adv Mater 2010;22(47):5424–30.
[69] Gent AN. Adhesion and strength of viscoelastic solids. Is there a relationship between adhesion and bulk properties? Langmuir 1996;12(19):4492–6.
[70] Wagoner M, Buttlar WG, Paulino GH, Blankenship P. Investigation of the fracture resistance of hot-mix asphalt concrete using a disk-shaped compact tension test. Transp Res Rec: J Transp Res Board 2005;1929:183–92.

[71] Williams JG. Visco-elastic and thermal effect on crack growth in PMAA. Int J Fract Mech 1972;8(4):393–401.
[72] Johnson FA, Radon JC. Molecular kinetics and the fracture of PMMA. Eng Fract Mech 1972;4:555–76.
[73] Maugis D. Review: subcritical crack growth, surface energy, fracture toughness, stick-slip and embrittlement. J Mater Sci 1985;20(9):3041–73.
[74] Webb TW, Aifantis EC. Oscillatory fracture in polymeric materials. Int J Solids Struct 1995;32(17–18):2725–43.
[75] de Gennes PG. Soft adhesives. Langmuir 1996;12(19):4497–500.
[76] Hui CY, Xu DB, Kramer EJ. A fracture model for a weak interface in a viscoelastic material (small scale yielding analysis). J Appl Phys 1992;72(8):3294–304.
[77] Park SW, Kim YR, Schapery RA. A viscoelastic continuum damage model and its application to uniaxial behavior of asphalt concrete. Mech Mater 1996;24:241–55.
[78] Park K, Paulino GH. Computational implementation of the PPR potential-based cohesive model in Abaqus: educational perspective. Eng Fract Mech 2012;93:239–62.
[79] Spring DW, Paulino GH. A growing library of three-dimensional cohesive elements for use in ABAQUS. Eng Fract Mech 2014;126:190–216.
[80] Makris N, Constantinou MC. Fractional-derivative Maxwell model for viscous dampers. J Struct Eng 1991;117:2708–24.
[81] Ruina A. Slip instability and state variable friction laws. J Geophys Res 1983;88(B12):10359–70.
[82] Serpieri R, Sacco E, Alfano G. A thermodynamically consistent derivation of a frictional-damage cohesive-zone model with different mode I and mode II fracture energies. Eur J Mech A/Solids 2015;2015:13–25.
[83] Parrinello F, Failla B, Borino G. Cohesive-frictional interface constitutive model. Int J Solids Struct 2009;46:2680–92.
[84] Parrinello F, Marannano G, Borino G. Mixed mode delamination analysis by a thermodynamically consistent cohesive interface model with independent mode I and mode II fracture energies. Procedia Eng 2015;109:327–37.
[85] Spring DW, Paulino GH. Computational homogenization of the debonding of particle reinforced composites: the role of interphases in interfaces. Comput Mater Sci 2015;109:209–24.
[86] Spring DW. Failure processes in soft and quasi-brittle materials with nonhomogeneous microstructures [Ph.D. thesis]. University of Illinois at Urbana-Champaign; 2015.
[87] Scott-Blair GW. The role of psychophysics in rheology. J Colloid Sci 1947;2(1):21–32.